small methods
www.small-methods.com

Mechanistic Insights into the Synthesis of Nickel-Graphene Nanostructures for Gas Sensors

*Chao Hsuan (Joseph) Sung, Bryan Yuji Gong, Haitao Yu, Sivasankara Rao Ede, Luz Cruz, Herry Fang, Ezra Sarmiento, Wenjie Zang, Geoffrey L. Barrows, and David Kisailus**

Toxic gases are used in different types of industries and thus, present a potential health hazard. Therefore, highly sensitive gas sensing materials are essential for the safety of those operating in their environments. A process involving electrospinning polymer solutions impregnated with transition metal ions are developed to yield nanofibers that are annealed to form graphitic carbon / nickel nanoparticle-based fibers for gas sensing applications. The performance of these gas sensors is strongly related to the ability to control the material parameters of the active material. As the formation of these nanostructures, which nucleate within solid carbon scaffolds, have not been investigated, the growth mechanisms are look to understand in order to exert control over the resulting material. Evaluation of these growth mechanisms are conducted through a combination of thermogravimetric analysis with mass spectrometry (TGA-MS), x-ray diffraction (XRD), scanning electron microscopy (SEM), transmission electron microscopy (TEM), and x-ray photoelectron spectroscopy (XPS) and reveal nucleation of nickel at the onset of the polymer scaffold decomposition with subsequent growth processes, including surface diffusion, aggregation, coalescence and evaporation condensation, that are activated at different temperatures. Gas sensing experiments conducted on analyte gases demonstrate good sensitivity and response times, and significant potential for use in other energy and environmental applications.

1. Introduction

Toxic gases are commonly used in different industries, thus present potential health hazards. Therefore, highly sensitive gas sensing materials are essential for the safety of those operating in their environments and technological developments are being utilized to approach human detection limits. The human nose consists of 400 different types of sensing cells with each type replicated over 100000 times, which allows for the biological olfactory system to detect gas analytes as low as tens of parts per billion (ppb).[1,2]

Gas sensors that are currently on the market primarily utilize vapor-sensitive polymers, semiconductor metal oxides, and other porous materials, such as silicon as the sensing material components. In recent years, semiconductor metal oxides have been studied extensively as the material component for gas sensors, owing to their high sensitivity, fast sensing response, prolonged stability, and simple implementation.[3,4] Furthermore, semiconductor metal oxides are especially promising due to the tunability of their functional properties depending on the chemical and structural characteristics, including chemical composition, surface defects, morphology, grain size, and specific surface area.[5] Such unique characteristics of metal oxides make them one of the most versatile and well-studied materials in the fields of semiconductor,[6] energy storage,[7] solar cells,[8] catalysis,[9,10] and magnetism.[11] However, conventional gas sensors that utilize semiconductor metal oxides often require elevated operating temperatures and require complex mechanisms, which leads to large power consumption and tedious maintenance procedures. These disadvantages of conventional semiconductor metal oxide gas sensors can be resolved by the utilization of nanostructured semiconductor metal oxide on microelectrochemical systems (MEMS).[12,13]

In 1991, Yamazoe et al. showed that such performance issues can be improved by the utilization of nanostructured metal oxides through a phenomenon deemed the "Grain Size Effect.[14]" In that research study, tin oxide was used as the sensing material and the nanostructured tin oxide sensing element produced by annealing at 700 °C had a particle size of 20 nm. Utilization

C. Hsuan (Joseph) Sung, B. Y. Gong, H. Yu, S. R. Ede, H. Fang, E. Sarmiento, W. Zang, D. Kisailus
Department of Materials Science and Engineering
University of California
Irvine, CA 92697, USA
E-mail: david.k@uci.edu

L. Cruz
Materials Science and Engineering Program
University of California
Riverside, CA 95251, USA

G. L. Barrows
Centeye Inc.
4905 Reno Road NW, Washington, D.C. 20008, USA

The ORCID identification number(s) for the author(s) of this article can be found under https://doi.org/10.1002/smtd.202400245

DOI: 10.1002/smtd.202400245

of nanostructured metal oxides in gas sensing application involves the ionosorption of oxygen species on the surface of the active material, which results in a charge depletion layer.[15–17] The change in resistance from analyte gas molecule adsorption is due to injection of charge carriers into the charge depletion layer.[18] The thickness of the depletion layer was reported to be 3 nm for sputtered SnO_2 film.[19] Yamazoe found that by lowering the annealing temperature, the crystallite size of SnO_2 is effectively reduced and the subsequent resistance and sensitivity of the sensing element were increased dramatically. The critical value of crystallite size is empirically determined to be twice the size of the depletion layer (6 nm in this case). This discovery allows detection of analyte gases without the use of a heating mechanism to induce sensing.

Many nanostructures, such as nanotubes, thin films, and nanofibers have been studied for the application of semiconductor metal oxide gas sensors. There have been various synthesis methods reported to fabricate active nanofiber-based material sensors in previous studies. For example, the vapor-liquid-solid (VLS) method has been reported to synthesize nanofibers consisting of indium (III) oxide,[20] gallium (III) oxide,[15] and vanadium (V) oxide.[21] In addition, templating methods, that use sacrificial nanoporous templates to guide the formation of nanostructures have been reported capable of synthesizing nanofibers consisting of metals,[22,23] conducting polymers,[24] semiconductors,[25] and metal oxides.[26,27]

The aforementioned methods of synthesizing metal oxide-based nanofibers, though powerful and effective, can be complicated and difficult to scale up in production. Electrospinning is a simple and versatile technique that due to recent commercial developments, can be used to produce large quantities of nanofibers.[28] This technique can be used to fabricate nanofibers from polymer solutions, gels, liquid crystals, melts, and emulsions. The use of polymer allows the synthesis of carbon/metal-based materials, which have been shown to exhibit great performance across myriad applications, including, biomedical,[29] photocatalytics,[30] photovoltaics,[31,32] field emissions,[33] energy storage,[34–37] catalysis,[38] and adsorption[39] due to their surface functionality,[40] high precision design, and porosity. There have been multiple reports regarding the synthesis of nanostructured metal oxides using electrospinning[41] and their subsequent performance in gas sensing. Since the performance of these sensors is directly related to the size and morphology of the constituent materials, it is critical to understand synthesis-structure relationships. The use of polymer matrices in the synthesis of nanostructured materials provides multiple benefits towards the resulting material properties in gas sensing applications. Beyond offering binding sites for metal cations, which controls supersaturation and thus nucleation and growth of metal nanoparticles, the resulting thermally decomposed carbonaceous structure provides sites for heterogenous nucleation,[42] prevents premature evaporation of nucleated nanoparticles at high temperatures,[43] and critically acts as a continuous, but porous, matrix to not only support the nanoparticles but also as a conductive element while allowing facile diffusion of analyte gases into and out of the sensing elements. A plethora of additional studies have been conducted to show the advantages of polymer-based-metal/metal oxide decorated nanofibers in gas sensing applications.[44] Moon et al. have shown promising sensing responses of TiO_2/polyvinylpyrrolidone (PVP) and Pd-doped TiO_2/PVP electrospun nanofibers against low concentration NO_2.[45] However, the relationships between synthesis and structure of nanoparticles in a polymer/carbon-based nanofiber matrix have yet to be studied. Furthermore, the utilization of these metal/carbon nanofibers are not limited to gas sensing. Tang et al. have shown promising characteristics of nanofiber materials in battery and catalyst applications,[46] which increases the importance of understanding the synthesis-structure relationship of these materials. Here, the nucleation and growth behavior of nickel nanoparticles in a polymer/carbon nanofiber matrix and their subsequent performance in gas sensing applications are described.

2. Results and Discussion

Here, we describe a method to synthesize nickel metal nanoparticle decorated carbon-based nanofibers, which involves a series of inorganic precursor – polymer solution mixing, electrospinning, and subsequent heat treatments (**Figure 1**). The homogeneous nature of the inorganic precursor – polymer solution ensures a uniform distribution of nanoparticles in subsequent annealed structures.

After spinning, but before annealing, SEM analysis demonstrate that no nanoparticles have formed. Subsequent oxidation, which was used to stabilize the polyacrylonitrile-based carbon structure via cyclization,[47] followed by annealing under reducing conditions, lead to the precipitation of nanoparticles in a carbon nanofiber matrix. Subsequent examination of these post-annealed structures (**Figure 2**) revealed the presence of nickel metal as well as graphene (at higher temperatures).

In order to gain control over the size and size distribution of these metal nanoparticles for creating effective gas sensors, it is important to understand their nucleation and growth behavior in a polymer/carbon matrix during thermal treatments. We thus conducted a systematic series of annealing experiments with subsequent material characterization. Samples were annealed at temperatures between 300 °C to 800 °C based on a previous report, showing the onset of polyacrylonitrile (PAN) decomposition occurs between 250 °C and 300 °C[48] as well as the authors personal experiences of nickel nanoparticle growth.

After annealing for 3 hours at increments from 300 °C – 800 °C, XRD was used to evaluate the resulting nanoparticle-based nanofibers (Figure 2).

Examination of the sample annealed at 300 °C reveals a small diffraction peak representative of (111) nickel, suggesting that the initial onset of nickel nanoparticle nucleation occurs around this temperature. Note that at annealing temperatures below 300 °C, no diffraction peaks were observed (see in-situ STEM experiment results below). With increasing annealing temperature, there is an increase in peak intensity and a subsequent decrease in peak width for nickel (111), (200), (220), and graphene (200). A significant change in peak intensity and sharpness for nickel can be observed between 500 °C and 600 °C, and beyond, suggesting significant growth within this temperature range.

Based on XRD data, it appears that the onset of nickel nanoparticle nucleation occurs by 300 °C. In order to examine this, the sample annealed at this temperature was subjected to TEM analysis. Selected area electron diffraction (Figure 2b) of nanofibers

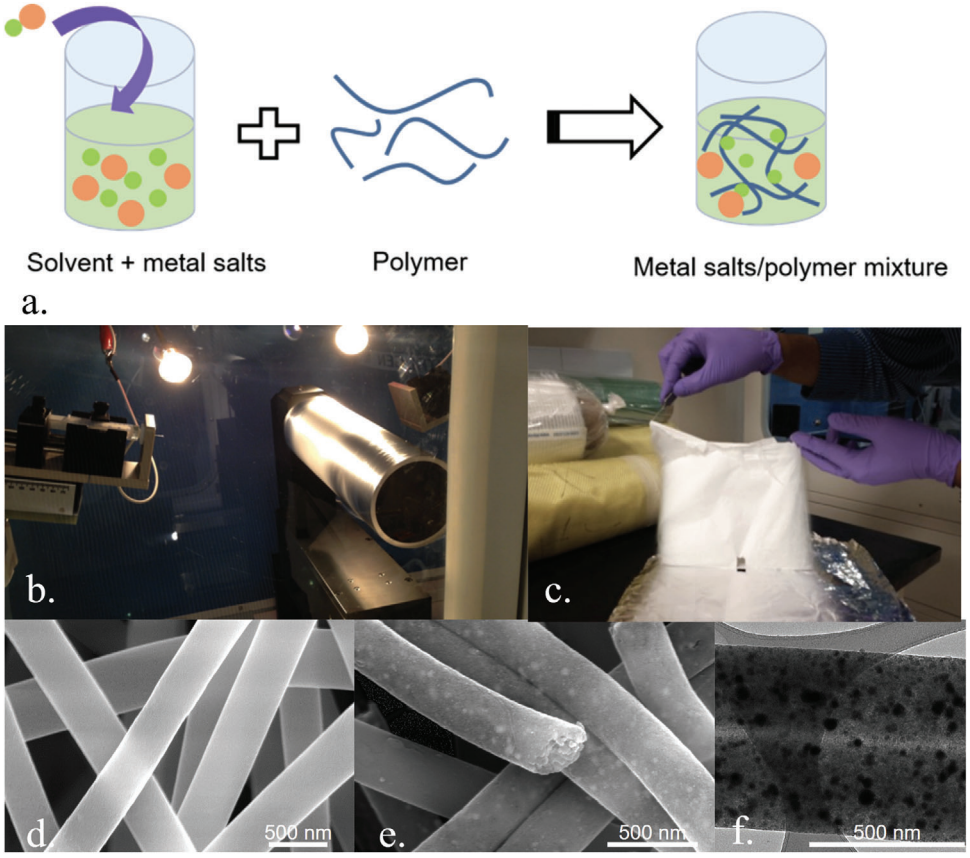

Figure 1. Schematic of synthesis of nickel-carbon nanofibers: a) mixing of precursor solution; b) electrospinning of nanofiber mats; c) resulting electrospun nanofiber mat; d. SEM micrograph of as-spun nanofibers; e) SEM micrograph of nanofibers after pre-oxidation and reduction heat treatment; f) TEM micrograph of pre-oxidized and reduced nanofibers.

annealed at 300 °C for 3 hours showed diffuse rings that were measured at 2.034 nm and 1.25 nm, corresponding to nickel (111) and (220) lattice planes, respectively. To visualize these very small nanoparticles, dark field TEM was conducted and uncovered ≈0.5 nm nanoparticles within the nanofiber matrix (Figure 2c). A closer examination of the dark field micrograph highlighted some regions where there appears to be alignment of these nanoparticles. While this was not observed throughout the entire sample, it is suggestive of regional sites where nucleation occurs within aligned pores, which could be a result of the polymer alignment during electrospinning. In fact, in the solution state, entangled polymer networks may experience substantial stretching and disentanglement because of the significant unidirectional forces parallel to the direction of the applied voltage during the electrospinning process.[49,50]

A similar alignment of nanoparticles was observed (Figure 2d) in nanofibers annealed at 400 °C for 4 hours. Due to the increased annealing temperature and longer dwell time, the nanoparticles were significantly larger than those annealed at 300 °C for 3 hours. It is important to note that although electrospinning provides potential polymeric chain disentanglement and subsequent nanoparticle alignment, there are likely regions where the distribution of polymer chains remain convoluted (similar to PAN in solution form).[51,52] Thus, the void space generated in those regions due to stabilization maybe more complex and why some fraction of nanoparticles observed are not aligned with each other.

In order to explain the onset of nucleation of nickel nanoparticles by 300 °C, thermo-gravimetric analysis, coupled with mass spectroscopy, was conducted on pre-oxidized nickel-PAN fibers to understand polymer behavior with temperature (**Figure 3**).

Analysis of these results revealed the onset of significant PAN decomposition at 285 °C, which coincides with the evolution of hydrogen cyanide. The significant mass loss above 285 °C coincided with the nucleation of nickel nanoparticles. This may be facilitated via the loss of coordination between nickel ions and the nitrile pendant groups contained within the polyacrylonitrile. Indeed, these nickel metal ions, which are present in the dissolved precursor solution, may form coordinated bonds with nitrogen atoms in the nitrile groups, resulting in the formation of nickel-nitrile metal-ligand complexes (R—C≡N—Ni).[53–55] The TGA-MS results that show the evolution of hydrogen cyanide during PAN decomposition have been demonstrated in previous work and have reported as the result of PAN cyclization.[47,56] Changes in polymer chemistry and structure with molecular rearrangements and mass loss during decomposition may enable nickel ions to more easily diffuse through this evolving polymer-carbon matrix, which can eventually lead to nucleation of nickel nanoparticles.

Examination by XPS of the nickel-PAN nanofibers was conducted, both before and after annealing in order to provide

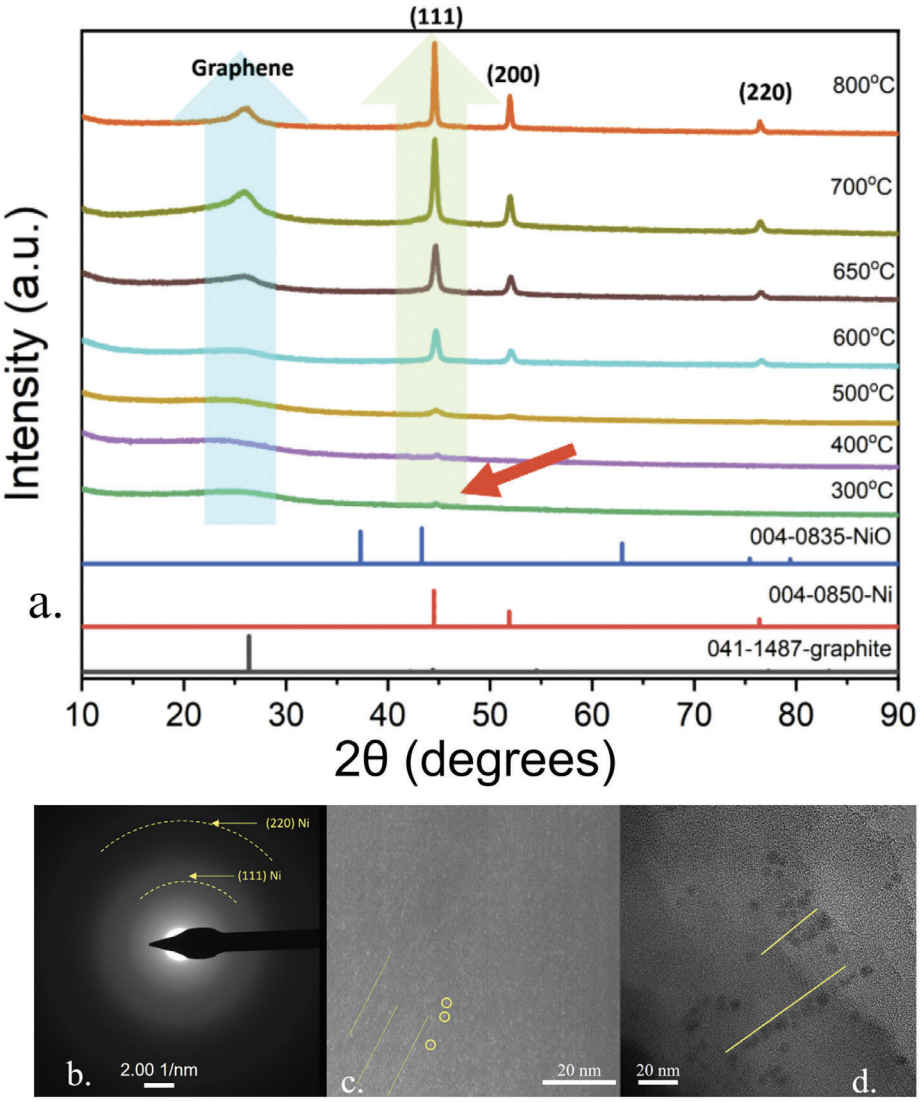

Figure 2. a) XRD analysis of nickel – polymer/carbon nanofibers annealed for 3 hours in reducing gas; b) selected area electron diffraction of nanofibers annealed at 300 °C for 3 hours; c) dark field TEM micrograph showing ≈0.5 nm nickel nanoparticles within carbon nanofibers annealed at 300 °C for 3 hours; d) bright field TEM micrograph of nickel nanoparticles within carbon nanofibers annealed at 400 °C for 4 hours.

information about the chemical nature of this system (**Figure 4**). The results show changes in the chemical state of carbon, nitrogen, and nickel.

Initial examination of the as-spun Ni-PAN fibers showed three C 1s binding energy peaks, 283.8, 285.3, and 287.3 eV, which are attributed to C-H, C-C, and C≡N bonds, respectively.[57–59] It is important to note that C 1s binding energies associated with carbon atoms in nickel acetate were not observed.[60] In addition, evaluation of the N 1s binding energy revealed a single peak centered at 398.2 eV. Previous reports of PAN have shown its N 1s binding energy centered at 399.0 eV,[61] and the decrease in this binding energy from metal-nitrile coordination,[62] thus, the N 1s peak observed for as-spun nanofibers is attributed nitrile N atoms coordinated with Ni ions (i.e., C≡N-Ni). Ni 2p binding showed two major peaks centered at 854.8 eV and 872.5 eV, which are attributed to Ni $2p_{3/2}$ and Ni $2p_{1/2}$ electrons, respectively.[63] Ni $2p_{3/2}$ and Ni $2p_{1/2}$ also exhibited two shakeup satellites.[64] The Ni 2p binding energy of nitrile coordinated Ni atoms is currently not understood, however, the binding energy of the Ni $2p_{3/2}$ peak observed here is in good agreement with a previous report on Ni coordinated with a dicyanamide anion,[65] suggesting Ni atoms are mostly coordinated with nitrile groups. It is also important to note that Ni atoms of nickel acetate exhibit similar binding energies,[60] thus, it is possible that the overall Ni 2p XPS spectrum observed here is a combination of both chemical states.

After pre-oxidization of the Ni-PAN nanofibers, significant changes to carbon, nitrogen and nickel binding energies were observed. Examination of C 1s binding energy revealed C-C (284.9 eV), C-N (286.5 eV), and C = O (288.8 eV) peaks,[46] while N 1s showed an overall 1.2 eV shift toward a greater binding energy and a doublet binding energy centered at 399.0 eV and 399.9 eV, corresponding to pyridinic N and pyrrolic N, respectively.[46] Emergence of pyridinic and pyrrolic N peaks are indicative of the chemical changes to PAN during cyclization, as shown by

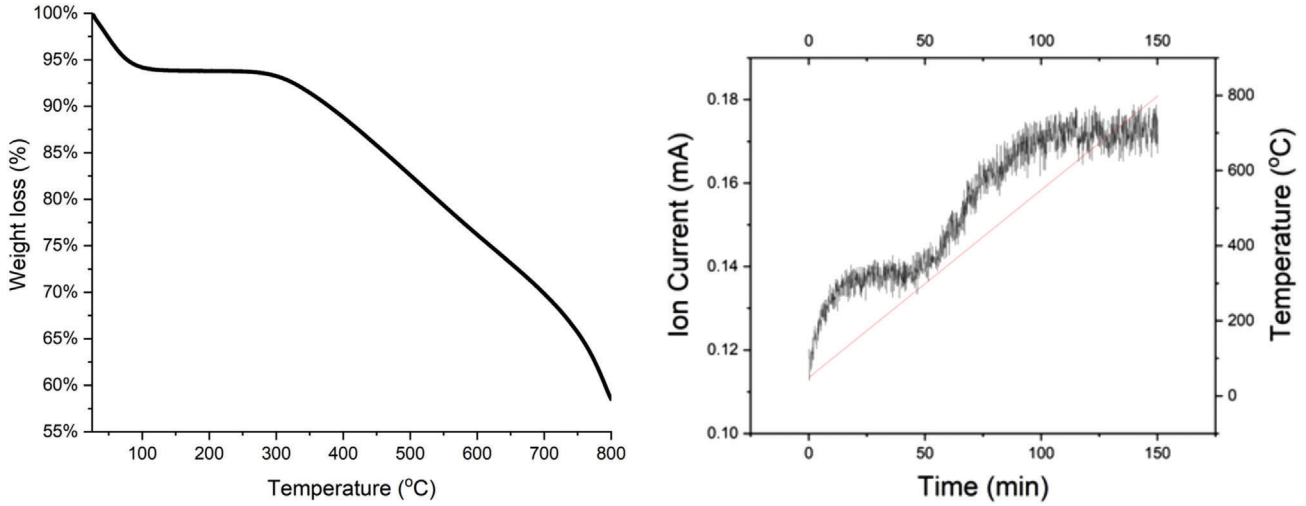

Figure 3. Thermo-gravimetric analysis of pre-oxidized nanofibers (left) and the associated mass spectrometry indicating hydrogen cyanide evolution at the same temperature as onset of PAN decomposition, 285 °C, (right).

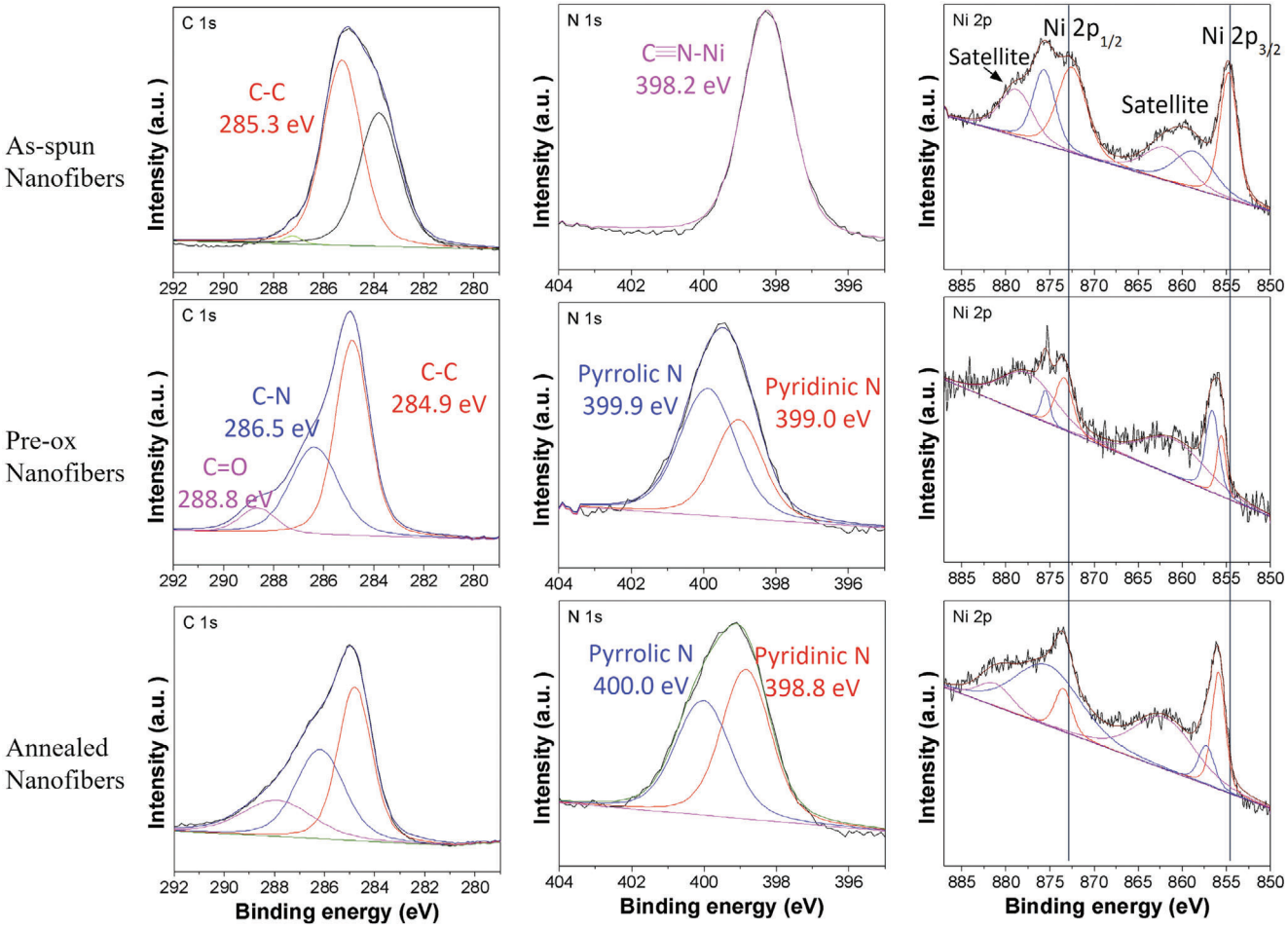

Figure 4. XPS spectra of C1s, N1s, and Ni 2p electrons of as-spun (top), pre-oxidized (middle), and annealed (300 °C) nanofibers (bottom).

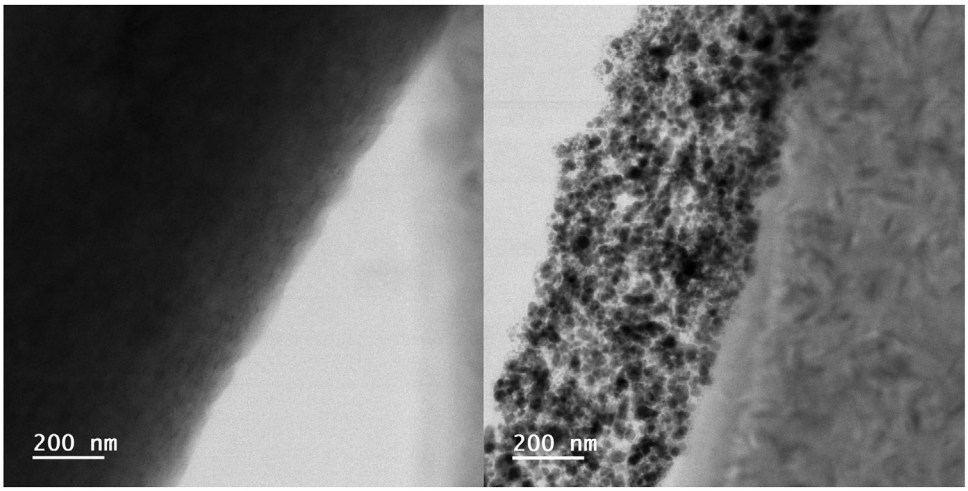

Figure 5. In situ STEM micrographs: (left) dark field micrograph of nanofibers at 300 °C in 5% H_2 / 95% N_2, (right) bright field micrograph of nanofibers at 400 °C in 5% H_2 / 95% N_2.

Tang et al..[46] Such a shift in binding energy is likely due to the change in chemical state of nitrogen atoms from one with greater screening due to higher negative valence charge density to one with lower screening, resulting in the decrease in kinetic energy of the ejected core level photoelectrons.[66] Therefore, it is likely that when PAN is cyclized, the change to a N-doped carbon ring structure resulted in a decrease in electron density near the nitrogen atom, perhaps due to π electron delocalization of cyclized PAN.[67] Furthermore, Ni $2p_{3/2}$ and $2p_{1/2}$ electrons each experienced a 1.2 eV and 0.9 eV shift, respectively, towards a greater binding energy, suggesting a decrease in local negative valence charge density of the different chemical states upon pre-oxidation. The Ni 2p binding energies are in close agreement with previous report on Ni atoms coordinated in the center of 4-pyridinic nitrogen.[68] It is likely that during the cyclization of PAN, interactions between Ni atoms and N atoms were weakened, enabling Ni atoms to freely diffuse. The concurrent formation of pyridinic nitrogen during PAN cyclization and detachment of Ni atoms, combined with enhanced diffusion at elevated temperatures,[69] likely resulted in the coordination between Ni and pyridinic N.

Upon annealing nanofibers at 300 °C, C 1s and N 1s binding energies remain largely unchanged, but it is worth noting that the relative concentration of pyridinic nitrogen increased significantly after annealing. These changes likely resulted in decreased polarity of the matrix and interactions between nickel atoms and nitrogen due to greater electron delocalization of the sp^2 hybridization of pyridinic N.[70] Thus, it appears that after a significant portion of PAN has been stabilized to form the N-doped carbon ring structure, there is a decrease in binding affinity between nickel and nitrogen (i.e., during the change from nitrile to pyridinic and/or pyrrolic nitrogen[46]), which enabled the nickel ions to more freely diffuse through the polymer/carbon matrix. Ni 2p binding of annealed nanofibers showed similar binding energies as pre-oxidized nanofibers. While a small shoulder exists on the lower binding energy side of the 855 eV peak, however, it is difficult to confirm the existence of substantial Ni-Ni bonding (852.6 eV[71]). It is likely that as there is an extremely low concentration and size (≈ 0.5 nm) of Ni nuclei in the polymer/carbon nanofibers, which is why no significant peak was observed. The concurrent partial decomposition of the polymer also enables the formation of pores, which can provide transport pathways in which these nickel ions can diffuse, leading to a kinetically enhanced process ultimately leading to nucleation of nickel nanoparticles.

In order to visualize the nucleation of nickel nanoparticles within the polymer/carbon nanofiber matrix, in situ scanning transmission electron microscopy (STEM) experiments were conducted. In situ gas cells (ProtoChip) were prepared using the same TEM preparation method as described with pre-oxidized nanofibers.

STEM micrographs of pre-oxidized Ni-PAN nanofibers were first obtained at 250 °C in an N_2 atmosphere, and showed no presence of nickel nanoparticles, suggesting that nucleation did not occur during the pre-oxidation. The gas flow was subsequently switched to 5% H_2 / 95% N_2 and the temperature was increased to 300 °C at 10 °C $second^{-1}$. A significant burst of nickel nanoparticles occurred almost instantaneously as the temperature reached 300 °C (**Figure 5**, left). It was observed that the nanoparticles experienced faster growth rates under these conditions compared to those prepared in the tube furnace, likely due to enhanced heating and gas diffusion rates in significantly smaller sample sizes (i.e., a few nanofibers versus thousands of compacted nanofiber mats), leading to facile polymer decomposition and subsequent metal ion diffusion processes (see Figures S3 and S4 (Supporting Information) for in situ STEM micrographs).

It is likely that the nucleation of nickel nanoparticles within this polymer matrix follows classical nucleation theory, wherein the nucleation is mostly dependent upon the supersaturation of the solute.[72] The timescale at which nucleation occurs, and the lack of nucleation of additional particles after the initial burst, suggests that particles initially form via a LaMer mechanism.[73] In the case of nickel nanoparticle formation within a polymer matrix, the increase in solute concentration is contributed by the detachment of nickel ions

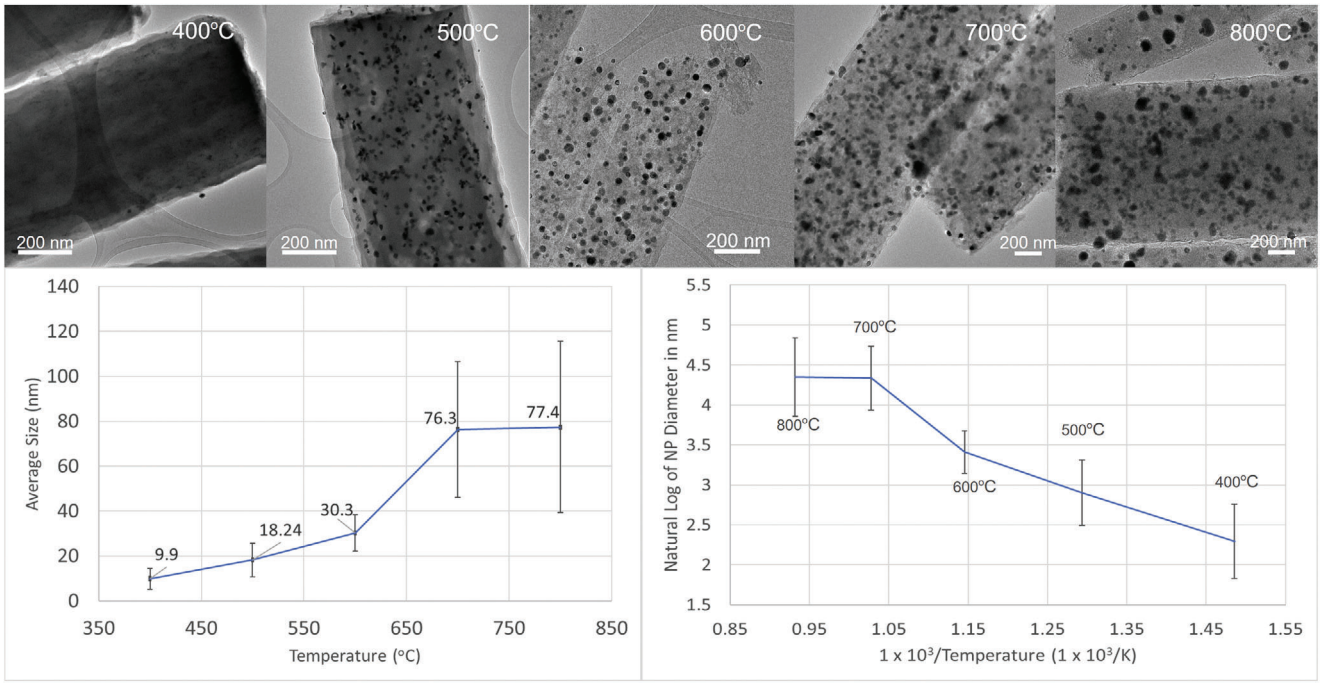

Figure 6. TEM micrographs of nanofibers annealed for 4 hours at different temperatures, graph of average particle size, and Arrhenius plot of average particle size.

during modification of pendant groups at temperatures around 300 °C.

It is important to note that most studies involved in metal nanoparticle nucleation and growth were conducted in vacuum or air without the presence of a secondary material matrix; the specific kinetics of metal nanoparticle growth within polymer or carbon matrices remains an understudied area. Thus, additional annealing steps were conducted on the nanofibers in order to understand metal nanoparticle growth behavior in this evolving carbonaceous matrix. TEM micrographs were obtained for a series of nanofibers that were annealed from 400 °C to 800 °C for 4 hours and the average particle sizes were obtained by 140 randomly selected particles per sample (**Figure 6**).

Analyses of particles annealed showed an expected increase in particle size with temperature, with significant changes in size occurring above 500 °C. For example, the average nickel nanoparticle at 400 °C was 9.9 nm ± 4.6 nm, but increased to 18.2 nm ± 7.5 nm at 500 °C. Interestingly, the nanoparticle alignment observed in samples heated to 300 °C is maintained at 400 °C and even up to 500 °C. Above this temperature, at 600 °C, the particle size (30.3 nm ± 8.1 nm) continues to increase at a similar rate as that observed from 400 °C to 500 °C, but the alignment of nanoparticles is lost and there is a noted decrease in the particle number density, likely due to coalescence of particles. Above 600 °C, the particle size changes are significant, increasing to 76.3 nm ± 30.3 nm by 700 °C. Interestingly, heating to 800 °C did not see a notable change in average particle size, but a broader size distribution (77.4 nm ± 38.1 nm). In fact, analysis of the particle size distributions between 700 °C and 800 °C (Figure S8, Supporting Information) demonstrate this significant broadening, not only with a cluster of larger particles (e.g., >120 nm), but also the addition of a number of particles less than 30 nm. While there is the possibility of nucleation of new particles at this high temperature, it is more likely that particles start to shrink in size, potentially via an evaporation-condensation mechanism, and will be discussed later.

According to Coble's theory, the relationship between activation energy and temperature of particle growth can be modeled by the Arrhenius equation,

$$\frac{d\ln k}{dT} = \frac{Q}{RT^2} \tag{1}$$

where k is the specific reaction rate constant, Q is the activation energy, R is the ideal gas constant, and T is the absolute temperature. Bolen et al. discovered that grain size is directly related to the activation energy through the integral of the Arrhenius equation:

$$\log D = \left(-\frac{Q}{2.303R}\right)\left(\frac{1}{T}\right) + A \tag{2}$$

where D is the grain size and A is the intercept. Thus, replotting the data as ln D versus $1/T$ and measuring the slope provided the activation energy, Q of the specific growth mechanism.[74] Previous reports have also used particle size in this calculation to derive the activation energy of growth mechanism of nanoparticles at different temperatures.[75,76] Evaluation of this plot with the corresponding TEM micrographs highlights a few potential growth mechanisms. At low temperatures (300 °C ≤ T < 500 °C), Ni nanoparticles likely grow through surface diffusion, wherein Ni atoms diffuse through the matrix and facilitate to particle growth via atomic addition. The activation energy derived from the Arrhenius equation at 400 °C – 500 °C was found to be 60.5 kJ mol^{-1}, which is similar to results reported by Panigrahi on

growth kinetics via surface diffusion in nickel nanopowders.[77] However, aggregation of nanoclusters cannot be ruled out as such structures were observed at 400 °C (Figure S5, Supporting Information).

Following the initial burst nucleation of Ni nanoparticles, residual concentrations of Ni ions exist in the nanofibers. STEM EDS conducted on regions of nanofibers (annealed at 800 °C for 4 hours, Figure S6, Supporting Information) void of nanoparticles indeed revealed the presence of significant quantities of Ni contained in the carbonaceous matrix. These results suggest that even after nucleation and prolonged periods of nanoparticle growth, the Ni content within the nanofiber was not exhausted during nucleation and growth. Previous reports have shown classical nanoparticle growth occurs via addition of monomers and aggregation, which involves diffusion of either solute atoms or nanoparticles, respectively.[78] Diffusion of entities at this length scale in solution state relies heavily on Brownian motion,[78] while diffusion within a solid matrix is dependent on metal-matrix interaction. Although experimental results showed the onset of PAN cyclization at 285 °C, it is possible that there are regions within nanofibers annealed at low temperatures that remain uncyclized or that open porosity is limited in some regions, resulting in localized nickel ions that are unable to diffuse and participate in nucleation. Limited research has been conducted on the interactions between single metal atoms and polymer pendant groups, but these interactions result in a barrier to metal ion diffusion through polymer networks.[69] Nevertheless, previous reports have investigated the relationship between metal reactivity and diffusivity within a polymer matrix and found that metals of low to intermediate reactivity with polymers tend to form clusters due to the metal-metal interactions being much stronger than metal-polymer interactions.[69,79] Under such circumstances, metal ions are relatively immobile, making long range diffusion challenging. The thermal energy supplied to the system at low temperatures may also be insufficient in activating mechanisms such as coalescence and evaporation. Furthermore, the elevated temperature above the glass transition temperature of PAN (87 °C–110 °C[80]) during annealing allows for greater degree of polymer diffusion which enhances solute and small nanoparticle (≈0.5 nm) diffusion.[69] For samples annealed at low temperatures, PAN cyclization and growth of Ni particles occurs concurrently. While as-spun PAN begins to cyclize, both cyclized and uncyclized regions of the matrix likely retain similar spatial distribution as the as-spun state, giving rise to the history dependence of the transport properties of Ni atoms,[69,81] wherein the polymer stretch and disentanglement during electrospinning likely resulted in anisotropic diffusional pathways for Ni ions. The diffusivity of Ni atoms and nanoparticles in polymer/carbon nanofibers is likely lower than those without a secondary material matrix. In fact, molecular dynamic simulations and experimental data have shown activation energies of Ni surface diffusion of unsupported Ni nanoparticles an order of magnitude lower than the calculated values from this study.[82] Thus, it is clear, the nanofiber matrix resulted in significant influence on the overall kinetics of nanoparticle growth at low annealing temperatures.

At high temperatures (>500 °C), TEM micrographs and the Arrhenius plot revealed a change in dominant growth mechanism from diffusion and aggregation to coalescence. Particle size distribution measurements also showed greater degree of polydispersity, specifically a bimodal distribution (Figure S8, Supporting Information), which is an indicator of coalescence.[72] Activation energies of Ni nanoparticle growth from 500 °C to 800 °C (in 100 °C intervals) are found to be 65.7 kJ mol^{-1}, 150.6 kJ mol^{-1}, and 2.8 kJ mol^{-1}, respectively. Calculated activation energies of Ni nanoparticle growth between 500 °C and 700 °C, a temperature range where coalescence mechanisms were activated, are in good agreement with previous report on Ni particle migration and coalescence.[83] The low activation energy between 700 °C and 800 °C may be attributed to the activation of evaporation, which will be discussed later. It is known that reduction in surface free energy of metal nanoparticles can be expected when embedded in a secondary material matrix.[43] Since the driving force of nanoparticle coalescence is widely agreed to be the decrease in surface energy from combining volumes and reduction of surface area of coalescing particles,[84–86] the rate of coalescence of Ni nanoparticles in the carbon nanofiber matrix is lower than Ni nanoparticles grown in vacuum. In fact, molecular dynamic simulations of nickel nanoparticle growth during high temperature sintering in vacuum shows that complete coalescence of two nanoparticles occur within nanoseconds.[87] Li et al. also showed the grain growth kinetics of nickel nanoparticles without a secondary material matrix and revealed accelerated growth (termed "unusual double growth" region) via coalescence between 500 °C and 600 °C,[88] which is 100 °C lower than what was observed in the carbon/polymer/nickel system studied here. These findings suggest that the carbon/polymer matrix significantly inhibited the relevant growth and coarsening kinetics of nickel nanoparticles, resulting in the delay of accelerated growth via coalescence. However, it is worth noting that although the presence of a solid matrix hinders nanoparticle growth, the higher surface free energy of unsupported nanoparticles when grown in vacuum results in greater degree of size dependent melting point depression,[89] therefore, it is likely that the polymer/carbon nanofiber matrix provides a more stable environment for nanoparticle growth.

The process of nanoparticle coalescence can be considered as initiated by nanoparticle diffusion, which is a thermally activated kinetic process,[84] wherein energy supplied to the system must be sufficient for nanoparticles to self-diffuse and make contact with other nanoparticles. The matrix material, in which nanoparticles diffuse, experienced chemical and structural changes with increasing temperature. As previously mentioned, Ni atoms and nanoparticles diffuse through regions of cyclized and uncyclized PAN at lower annealing temperatures; however, at higher temperatures, most of the PAN content is cyclized. Furthermore, TEM micrographs and XRD data reveal significant quantities of turbostratic carbon and graphene present in nanofibers annealed at temperatures above 600 °C. The transport properties of Ni atoms and nanoparticles through graphitized nanofibers are dependent on the interactions between carbon and nickel. A previous report has shown an increase in metal-carbon interactions leads to a decrease in metal diffusivity through graphitic matrices.[90] It is likely that the change in surface environment of the matrix material (i.e., PAN → cyclized PAN → carbon/graphitic matrix) as annealing temperatures are increased, resulting in the decreased interactions between nickel nanoparticles and the nanofiber matrix, which effectively lowers the activation barrier for coalescence. During in situ STEM

experiments (Figure 5, right), enhanced polymer decomposition due to the small sample size and increased growth were observed concurrently with nanoparticles coalescing at 400 °C, suggesting that nanoparticle coalescence depends greatly on the state of the nanofiber matrix.

Clearly, the melting point depression effect of these nanoparticles also controls their coalescent behavior. Teijlingen et al. have shown the size-dependent melting point depression of nickel nanoparticles below 6 nm via dynamic TEM.[91] This allows the formation of a surface molten layer, thus making coalescence of nanoparticles possible via particle fusion more facile.[84] It is likely that coalescence could be activated at temperatures as low as 500 °C, where the particle size (< 20 nm) affected the melting temperature of these materials.

As mentioned previously, there is little change in average nanoparticle size between samples annealed at 700 °C and 800 °C for 4 hours. As discussed, the particle size distribution is broadening (Figure S6, Supporting Information), not only with larger sized particles, but with smaller particle sizes identified. At 800 °C, the small particles have a significant curvature and can undergo evaporation via the Kelvin effect.[92] Previous reports have shown evaporation of nanoparticles occur at lower temperatures compared to bulk materials due to the inverse relationship between nanoparticle size and vapor pressure.[43,93,94] As nanoparticle sizes decrease, vapor pressures increase, which causes nanoparticles to evaporate more easily relative to bulk materials. It is likely that at high temperatures, the vapor pressure of these nanoparticles was sufficient to induce evaporation, reducing the size of nickel nanoparticles, resulting in graphitic "onion rings" (i.e., hollow structures formerly containing nickel) or incomplete evaporation resulting in an increase in the number of particles < 30 nm. It is also worth noting that evaporation of Ni nanoparticles on the surfaces of the nanofibers may occur faster than those in the interior due to enhanced kinetics at the surfaces of the nanofibers. Verification of the evaporation of Ni nanoparticles was conducted by exposing a single-crystalline Si wafer to gas flow downstream from the nanofiber sample while annealing at 800 °C for 5 hours. This resulted in the formation of a black film being deposited on the Si wafer, which was subsequently analyzed via XRD (Figure S9, Supporting Information). The XRD spectrum revealed nickel metal peaks, confirming that nickel nanoparticles were evaporated from the nanofiber matrix and condensed back onto the silicon wafer as a nickel metal film.

In addition to particle coalescence, two more mechanisms were observed in nanofibers annealed at high temperatures: formation of turbostratic graphene (t-graphene) and evaporation of nanoparticles. T-graphene was observed in the form of ring like structures around nickel nanoparticles (**Figure** 7a), or empty graphene rings distributed throughout the nanofiber (Figure 7b). FFT patterns of Figure 7a and b both reveal a ring measured at 3.345 nm corresponding to the interlayer spacing of t-graphene.[95]

The exact mechanism of t-graphene formation in this system requires further investigation, but nickel nanoparticles are likely responsible for catalyzing such formation as they have shown to be effective catalysts for t-graphene and graphene formation.[96,97] It is likely that the carbonaceous species outgassed during annealing[98] provided the carbon source for graphene/t-graphene formation via an "induction" process into the nickel nanoparticles which subsequently nucleate on the nanoparticle surface.

The empty t-graphene rings in Figure 7b suggest that the nickel nanoparticles that were previously observed had evaporated. This can be seen as the amount of empty t-graphene rings increases with the annealing time at high temperatures. It is clear that a number of growth mechanisms were activated from the as-spun fiber formation through the annealing process. A schematic provided illustrates the observations discussed herein (Figure S10, Supporting Information). Further investigation into the mechanisms of graphitic formation and their role in particle growth are underway.

2.1. Gas Sensing

As previously mentioned, for gas sensing applications, nanofibers containing sub-10 nm nanoparticles and high porosity possess enhanced sensing capabilities; however, these two characteristics are achieved at separate annealing temperatures. The aforementioned observations demonstrate that carbon-based nanofibers containing nickel nanoparticles are relatively monodispersed with controlled diameters are synthesized at temperatures below 500 °C. However, the density of the evolving polymer / carbon matrix remains high, which inhibits analyte gas molecule diffusion to sensing elements, effectively reducing the sensitivity of these sensors. Conversely, the same nanofibers annealed above 600 °C possess significant porosity, but the nanoparticles within are large and can be highly polydisperse, also reducing performance of sensors.

Due to these challenges, the annealing schedule must be specifically tuned to synthesize nanoparticle decorated nanofibers with both controlled particle sizes and significant porosity. Because nanoparticle sizes depend on both annealing temperature and duration, we devised the following annealing schedule: pre-oxidation at 250 °C for 4 hours (ramp rate: 2 °C min^{-1}), followed by heating to 700 °C at a high rate (i.e., 20 °C min^{-1}) for a short hold time (20 mins). The combination of a high annealing temperature, a fast ramp rate, and a short dwell time allowed effective control over nanoparticle size, while generating greater porosity to create diffusional pathways for analyte gas molecules (sample denoted as Ni/PAN). Additionally, since gas sensing of metal/metal oxide nanomaterials involves the change in resistance of the active material from the adsorption and desorption of analyte gas molecules,[16,44] the conductivity of the nanofibers is also an important factor that influences response time. The use of high temperature annealing promotes the graphitization of the nanofibers, effectively increasing the conductivity of the nanofibers and decrease the response time. Thus, nanofibers with relatively small particles and great porosity were synthesized (Figure S11, Supporting Information). These materials were subsequently evaluated in gas sensing experiments via measurements of electrical resistance during exposure to ammonia analyte gases. Here, the nanofiber-mounted sensor board (Figure S1, Supporting Information) was secured in the gas chamber, and subsequently subjected to a 5-minute N_2 (at 1 standard liter per minute, SLPM) purging cycle to allow for stabilization of the resistance, which settled at ≈1050.7 Ω. This value served as the baseline resistance for

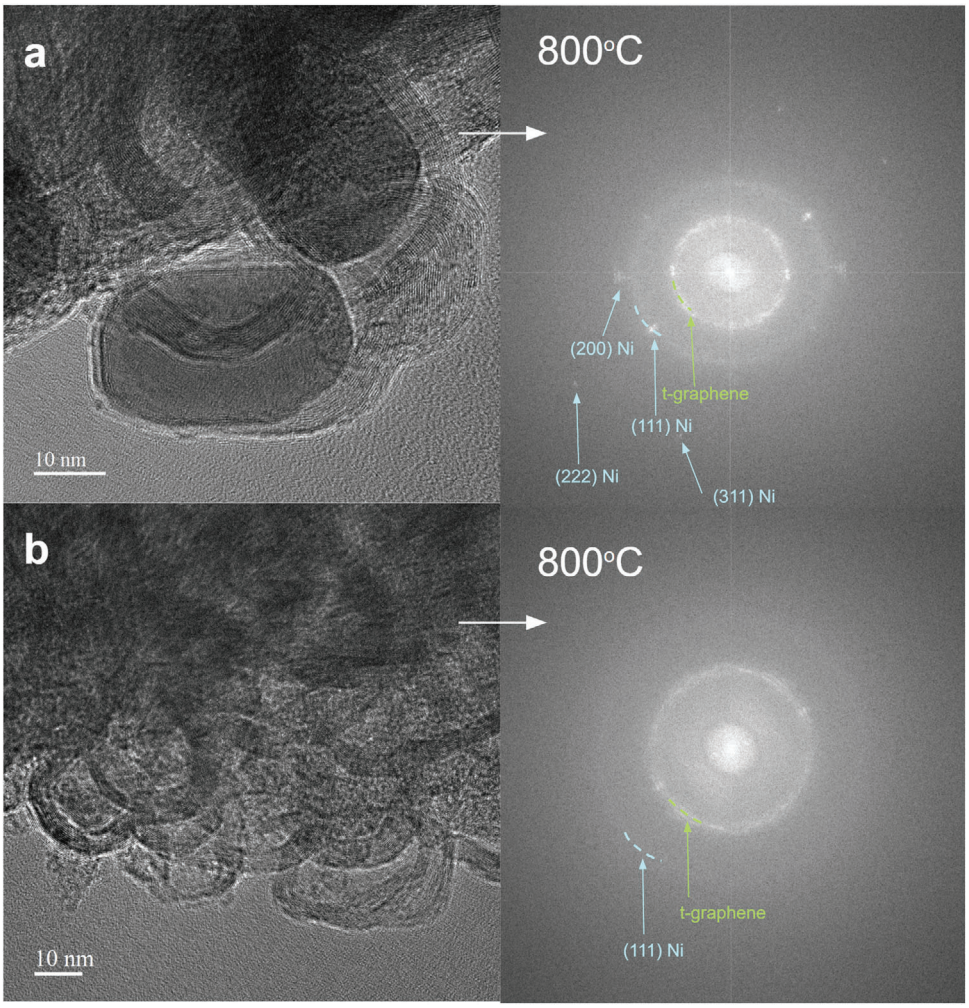

Figure 7. TEM micrographs and Fast Fourier Transform (FFT) of a) turbostratic graphene rings around nanoparticles found in samples annealed at 800 °C; b) empty turbostratic graphene rings found in samples annealed at 800 °C.

subsequent calculations. During this gas sensing experiment, the sensor board was exposed to 1000 parts per million (ppm) ammonia (NH_3) six times: the first two intervals had 1 minute durations, the third and fourth intervals were at 3 minutes each, and the last two intervals were at 5 minutes each. After each NH_3 exposure interval, an N_2 purging cycle of equal duration was carried out to observe recovery performance of the nanofibers. All gas sensing experiments were conducted at room temperature (23 °C). The gas sensing performance of this sample against 1000 ppm NH_3 (at 0.2 SLPM) is shown in **Figure** 8a.

The changes in resistance showed patterned responses, which can be accurately interpreted to detect analyte gases. Resistance changes during NH_3 exposure intervals exhibited logarithmic growth, which is likely due to the self-diffusion behavior of NH_3 molecules.[99,100] The absolute change in resistance during NH_3 exposure intervals (relative to the resistance settled at the end of the preceding N_2 purging interval), the percent change (calculated by dividing absolute change during NH_3 exposure intervals with the resistance settled at the end of the preceding N_2 purging interval), the absolute change in resistance during N_2 purging intervals, and percent recovered (calculated by dividing absolute change during N_2 purging intervals with the absolute change in resistance during the previous NH_3 exposure interval) are given in the table on the right side of Figure 8.

The sample analyzed in Figure 8 showed a moderate rate of recovery; however, as NH_3 exposure times increased, the percent recovery during each subsequent purging cycles decreased, indicating difficulty in desorption of NH_3 molecules within the nanofibers. To mitigate this issue, we attempted to engineer nanofibers with greater porosity by introducing poly(vinyl pyrrolidone) (PVP) into the electrospinning solution.

Thus, Ni-nanoparticle based nanofibers were synthesized from a Ni/PAN/PVP/ (4:1 PAN to PVP weight ratio) solution and annealed at 700 °C for 30 mins at a ramp rate of 10 °C min^{-1}. In addition, the sample was removed from the hot zone of the tube furnace immediately after the 30 mins dwell time to allow for faster cooling (sample denoted as Ni/PAN/PVP). Due to the lower thermal stability of PVP relative to cyclized PAN,[101] it was hypothesized that as the annealing temperature increases above 400 °C, the PVP in the nanofiber matrix will decompose to form additional porosity (TEM micrographs of this sample are shown

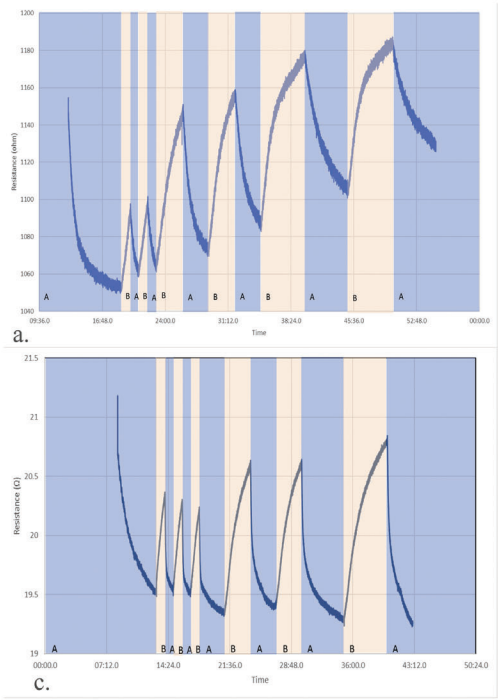

	Change in Resistance (Ω)	% Change		Resistance Recovered (Ω)	% Recovered
NH_3 (1)	48.9	4.5	N_2 (1)	37.4	80.8
NH_3 (2)	41.1	3.9	N_2 (2)	39.5	79.2
NH_3 (3)	88.9	8.4	N_2 (3)	80.9	81.5
NH_3 (4)	89.1	8.3	N_2 (4)	74.9	69.4
NH_3 (5)	97.4	8.9	N_2 (5)	77.9	60.2
NH_3 (6)	85.1	7.9	N_2 (6)	61.7	45.2

	Change in Resistance (Ω)	% Change		Resistance Recovered (Ω)	% Recovered
NH_3 (1)	0.88	4.5	N_2 (1)	0.87	101
NH_3 (2)	0.79	4.1	N_2 (2)	0.82	103
NH_3 (3)	0.74	3.8	N_2 (3)	0.89	124
NH_3 (4)	1.31	6.7	N_2 (4)	1.23	110
NH_3 (5)	1.25	6.4	N_2 (5)	1.39	123
NH_3 (6)	1.58	8.2	N_2 (6)	1.61	120

Figure 8. Gas sensing resistance plot, nanoparticle size distribution, and table of gas sensing data of Ni/PAN nanofibers annealed at 700 °C for 20 mins at 20 °C min^{-1} (top) and Ni/PAN/PVP based nanofibers.

in Figure S10, Supporting Information). Here, samples were exposed to 1000 ppm NH_3 where the first three exposure intervals were at 1 minute each in duration, the fourth and fifth were at 3 minutes each, while the sixth interval was at 5 minutes. The sensing response of this sample (Figure 8c) showed patterned resistance changes during purging and exposure intervals. After the initial 5 minutes of a N_2 purging cycle, the resistance settled at roughly 19.5 Ω (set as baseline). During each NH_3 exposure interval, resistance increased by following a logarithmic growth profile. Unlike the sample without PVP, during the first three exposure intervals, the change in resistance decreased, indicating slight fatigue in sensing responses. During each N_2 purging interval, complete recovery of the resistance changes that occurred in the previous NH_3 exposure interval was observed. This indicates that the adsorption and desorption of NH_3 molecules occur at similar rates, which is advantageous for signal recognition in the future for direct correlation between resistance changes with concentration of analyte gas. It is also important to note that during purging, the resistance changes follow an exponential decay profile. During purging intervals, as time progresses, desorption of analyte molecules on nanoparticle surfaces may follow collision-based kinetics,[102,103] such that N_2 molecules collide with NH_3 molecules, resulting in molecule knockoff. As such, molecules that are adsorbed to nanoparticle surfaces that are closer to the nanofiber surface desorb more quickly, leaving behind NH_3 molecules that are difficult for N_2 molecules to reach.

XPS characterization was conducted to investigate the surface chemistry of the nanofibers tested during gas sensing experiments (Figures S13 and S14, Supporting Information). Analysis of this data revealed the presence of oxygen and additional adsorbates, which would affect the sensing performance. In fact, additional variables, such as oxygen concentration and relative humidity, which have been reported to affect sensor responses,[104,105] will also be investigated in future work. Surface area and porosimetry were also conducted with N_2 adsorption isotherm experiments, which revealed slight differences in the specific surface area and minimal differences in pore distributions (Figure S15, Supporting Information). Calculated Brunauer, Emmett and Teller (BET) specific surface areas[106] of Ni/PAN and Ni/PAN/PVP were 374.93 $m^2 g^{-1}$ and 346.27 $m^2 g^{-1}$, respectively. Porosity of both samples were limited to the micropore ranges, evident from the early onset plateau of the adsorption isotherm. Horvath-Kawazoe differential pore volume plots[107] revealed similar pore distributions between the two samples. Thus, it is likely that the difference in sensing performances are attributed to the difference in surface chemistry of the two samples. As shown in the Ni 2p and O 1s binding energies of both samples, the surface environments are different, with Ni/PAN/PVP possessing a significantly larger concentration of Ni metal and surface adsorbed CO_2, while Ni/PAN had larger concentrations of what appear to be NiOOH and surface adsorbed O_2. Adsorbate species have been shown to influence sensing mechanisms and performances dramatically,[108] thus further studies are being conducted on their role in selectivity and recovery in gas sensors. Beyond this, we are now investigating the same materials for use in energy storage and conversion systems.

3. Conclusion

Ni-based polymer / carbon nanofibers were synthesized through a solution mixing, electrospinning, and annealing process. Investigation into the evolution of the nanofiber at different stages

of heating revealed the transition of the matrix material from PAN to cyclized PAN at low temperatures, and to graphitic carbon at high temperatures, resulting in the change in chemical environment of Ni atoms within the nanofibers. Direct correlation between these changes and the nucleation of Ni nanoparticles were made based on XPS results of as-spun, pre-oxidized, and annealed nanofibers. Subsequent analysis of the TEM micrographs of nanofibers annealed at different temperatures revealed the change in growth mechanism from surface diffusion and aggregation at low temperatures, to coalescence and evaporation-condensation at high temperatures. Ni-based polymer / carbon nanofibers were subjected to gas sensing experiments against 1000 ppm NH_3 and exhibited good gas sensing performance, validating efforts of continued research and engineering of these nanofibers in future gas sensing, as well as energy conversion and storage applications.

4. Experimental Section

Synthesis of Nanofibers: *Precursor Solution*: Dimethylformamide of 8.8 g, 0.25 g of nickel acetate tetrahydrate, and 1.2 g of polyacrylonitrile, all purchased from Sigma Aldrich, were mixed into a solution on a stir plate. The solution was mixed for 6 hours at 80 °C at a stir rate of 350 rpm. Subsequently, the temperature and stir rate were decreased to 25 °C and 150 rpm respectively, and mixing was continued for an additional 12 hours.

Electrospinning: Electrospinning was conducted with a NanoNC eSrobot Electrospinning/spray system (Model: ESR200PR2D). The aforementioned precursor solution was placed in a syringe with a needle and was loaded in the electrospinner. The voltage was set at -5 kV and 10 kV (i.e., a voltage offset of 15 kV) and the injection rate was set to 0.8 mL h^{-1}. Fibers were then spun onto a piece (12×4 inches) of aluminum foil over a period of 4 hours to yield nanofiber mats, which were left to dry in ambient air for at least 24 hours.

Heat Treatments: As-spun nanofibers were cut into ≈1.25×10 cm strips, two of which (roughly 50–70 mg) were placed into an alumina boat for annealing in a tube furnace. For nickel/PAN nanofibers, subsequent annealing was conducted in two steps: oxidation and reduction. For oxidation heat treatments, as-spun fibers were heated from 25 °C to 250 °C at 2 °C min^{-1}, and held for 4 hours in air at 150 cc min^{-1}. For reduction processing, samples subjected to oxidation treatments were heated from 25 °C to the target temperature at 5 °C min^{-1}, and held at different times in 5% H_2/95% N_2 reducing gas at 150 cc min^{-1}.

Characterization of Nanofibers: *X-ray Diffraction (XRD)*: Heat-treated nanofibers were characterized using powder x-ray diffraction (XRD) with a Rigaku SmartLab X-Ray Diffractometer (Tokyo, Japan) with a Cu Kα anode operated at 40 kV and 30 mA. Nanofiber samples were grounded with an agate mortar and pestle for 15 minutes and placed on a zero background silicon holder. The ground samples were subsequently flattened using a glass slide to ensure accurate data capture. XRD experiments were conducted at a scan rate of 0.5°/minute from 2θ angle 20° to 80°.

X-ray Photoelectron Spectroscopy (XPS): The surface composition and chemical states of Carbon (C), Nitrogen (N), and Nickel (Ni) were characterized using X-ray photoelectron spectroscopy (XPS) with an XPS/UVS-SPECS system (Berlin, Germany) featuring a PHOIBOS 150 analyzer under a pressure of ≈ 3×10^{-10} mbar. The instrument utilizes Mg Kα X-ray (hν = 1253.6 eV) and Al Kα X-ray (hν = 1486.7 eV) sources. The data were acquired using the Mg Kα X-ray source, which was operated at 10 kV and 30 mA (300 W) and analyzed with the CasaXPS software. XPS spectra of the survey scan were recorded with a pass energy of 24 eV in a 0.5 eV step. The surface composition and chemical states of carbon, nitrogen, oxygen, and nickel of nanofibers utilized in gas sensing experiments were characterized using XPS on a Kratos-AXIS-Supra instrument, equipped with a monochromatic Al K-alpha x-ray source at a power of 225 W. The vacuum of the characterization chamber was maintained at below 5E-08 torr during data acquisition. Survey scans was recorded using a pass energy of 160 eV, 100 ms dwell time and 1 eV stepsize. Detailed spectra of C 1s, N 1s, O 1s, and Ni 2p were averaged from 15 sweeps using a 20 eV pass energy, 100 ms dwell time, and a 0.1 eV stepsize.

Transmission Electron Microscopy (TEM) and Energy Dispersive Spectroscopy (EDS): Heat-treated nanofibers were examined using a JEOL-2800 transmission electron microscope operated at an accelerating voltage of 200 kV. Samples were ground with an agate mortar and pestle for 10 minutes and placed in a 2 mL plastic vial. Ethanol was then added to the vial and the nanofiber/ethanol suspension was subsequently tip sonicated for 30 seconds. The sonicated suspensions were deposited onto a TEM copper grid (Ted Pella lacey carbon 400 mesh) and let dry in ambient environment for at least 12 hours before TEM analyses. EDS experiments were conducted in scanning transmission electron microscope (STEM) mode with the same sample preparation, instrument, and accelerating voltage. STEM and EDS detectors were used for microscope alignment, spectral data acquisition, and EDS mapping.

Scanning Electron Microscopy (SEM): The morphologies of heat-treated nanofibers were examined using a TESCAN MIRA3 GMU FESEM (Brno, Czech Republic) at an accelerating voltage of 15 kV. In order to prepare samples for imaging, a few drops of the aforementioned nanofiber/ethanol suspension (see TEM section) were placed onto a piece of carbon tape, which was placed on a SEM stub and allowed to dry at room temperature.

Thermogravimetric Analysis – Mass Spectroscopy (TGA/MS): Pre-oxidized nanofibers were characterized by TGA/MS with a Discovery TGA Thermogravimetric Analyzer with Mass Spectrometry accessory. Grounded sample of 2 mg was loaded into an alumina sample cup and underwent a two-step heating process using a 5% H_2 / 95% N_2 gas mixture to simulate the reduction environment used in other annealing experiments. Specifically, samples were heated according from: (i) 25 °C – 100 °C at 200 °C min^{-1} and then (ii) 100 °C to 800 °C at 5 °C min^{-1}. Data acquisition via both TGA and MS was collected from 50 °C to 800 °C in order to understand the mass loss behavior and gaseous species evolution during heating.

Surface Area and Pore Size Analysis: Surface area and pore size analysis were conducted via N_2 adsorption isotherm experiments with the Micromeritics 3Flex instrument (Norcross, USA). Samples were grounded with a mortar and pestle for 5 minutes and subsequently degassed at 200 °C for 6 hours. Surface area values were calculated based on Brunauer-Emmett-Teller (BET) theory and pore size distributions were calculated based on Horvath-Kawazoe (HK) theory.

Fabrication of Sensor Boards: The microelectrochemical system (MEMS) used in this research were provided by Centeye, Inc. (Washington, D.C., USA). This system consisted of a sensor board and a Teensy board (See Figure S1, Supporting Information), connected by wires. Silver epoxy (MG Chemicals 8330S) was applied to the sensor board electrode contact with a stencil, after which roughly 5 µg nanofibers were mounted on the sensor board electrode contact. The sensor boards were subsequently heated to 65 °C in air to cure the silver epoxy. The board was then left to dry for 24 hours before gas sensing experiments were conducted. Sensor board dimensions were shown in Figure S2 (Supporting Information).

Supporting Information

Supporting Information is available from the Wiley Online Library or from the author.

Acknowledgements

The authors acknowledge funding from Air Force Research Labs, Grant # FA864920C0314. The authors also wish to acknowledge Dr. Amanda Strom from the Materials Research Lab at the University of California, Santa Barbara, for help with Thermogravimetric Analysis-Mass Spectroscopy as well as the use of the Analytical Instrumentation Facility (AIF) at North Carolina State University, which was supported by the State of North Carolina and the National Science Foundation.

Conflict of Interest

The authors declare no conflict of interest.

Data Availability Statement

The data that support the findings of this study are available from the corresponding author upon reasonable request.

Keywords

crystal growth, gas sensing, graphene, nanostructured materials, nucleation

Received: February 19, 2024
Revised: April 17, 2024
Published online: May 19, 2024

[1] Y. Dan, S. Evoy, A. T. C. Johnson, Chemical Gas Sensors Based on Nanowires, https://arxiv.org/pdf/0804.4828.
[2] R. H. Wright, *The Science of Smell*, Geo. Allen & Unwin Ltd, London **1964**.
[3] S. J. Patil, A. V. Patil, C. G. Dighavkar, K. S. Thakare, R. Y. Borase, S. J. Nandre, N. G. Deshpande, R. R. Ahire, *Front. Mater. Sci.* **2015**, *9*, 14.
[4] O. Berger, T. Hoffmann, V. Melev, *J. Mater. Sci.: Mater. Electron.* **2004**, *15*, 483.
[5] B. Saruhan, R. Lontio Fomekong, S. Nahirniak, *Front. Sens.* **2021**, *2*, 657931.
[6] Z. Dong, X. Lai, J. E. Halpert, N. Yang, L. Yi, J. Zhai, D. Wang, Z. Tang, L. Jiang, *Adv. Mater.* **2012**, *24*, 1046.
[7] Z. Shao, Q. Zhu, Y. Sun, Y. Zhang, Y. Jiang, S. Deng, W. Zhang, K. Huang, S. Feng, *Adv. Mater.* **2022**, *34*, 2110172.
[8] Y. Yang, Q. Jin, D. Mao, J. Qi, Y. Wei, R. Yu, A. Li, S. Li, H. Zhao, Y. Ma, L. Wang, W. Hu, D. Wang, *Adv. Mater.* **2017**, *29*, 1604795.
[9] H. Wang, D. Mao, J. Qi, Q. Zhang, X. Ma, S. Song, L. Gu, R. Yu, D. Wang, *Adv. Funct. Mater.* **2019**, *29*, 1806588.
[10] K. Huang, Y. Sun, Y. Zhang, X. Wang, W. Zhang, S. Feng, *Adv. Mater.* **2019**, *31*, 1801430.
[11] Z. R. Dai, Z. W. Pan, Z. L. Wang, *Adv. Funct. Mater.* **2003**, *13*, 9.
[12] S. Chandra, H. Pandya, A. Vyas *Integration of MEMS with Nanostructured Metal-Oxide Materials for Improved Sensors for Volatile Organic Compounds* (Eds: M. Katiyar, B. Mazhari, Y. N. Mohapatra), Proc. SPIE 8549, 16th International Workshop on Physcics of Semicoductor Devices, 854919 (15 October 2012).
[13] G. Niu, F. Wang, *J. Micromech. Microeng.* **2022**, *32*, 054003.
[14] N. Yamazoe, *Sens. Actuators B Chem.* **1991**, *5*, 7.
[15] M.-F. Yu, M. Z. Atashbar, X. Chen, *IEEE Sens. J.* **2005**, *5*, 20.
[16] N. Bârsan, M. Huebner, U. Weimar, in *Semiconductor Gas Sensors*, Elsevier, Amsterdam **2020**, pp. 39–69.
[17] B. Saruhan, A. Yüce, Y. Gönüllü, K. Kelm, *Sens. Actuators B Chem.* **2013**, *187*, 586.
[18] D. Degler, U. Weimar, N. Barsan, *ACS Sens* **2019**, *4*, 2228.
[19] H. Ogawa, M. Nishikawa, A. Abe, *J. Appl. Phys.* **1982**, *53*, 4448.
[20] D. Zhang, Z. Liu, C. Li, T. Tang, X. Liu, S. Han, B. Lei, C. Zhou, *Nano Lett* **2004**, *4*, 1919.
[21] V. O. Nanofibres, *Sens. Actuators B Chem.* **2005**, *106*, 730.
[22] R. B. Sadeghian, M. Kahrizi, *Sens. Actuators Phys.* **2007**, *137*, 248.
[23] Z. Liu, P. C. Searson, *J. Phys. Chem. B* **2006**, *110*, 4318.
[24] Y. Dan, Y. Cao, T. E. Mallouk, A. T. Johnson, S. Evoy, *Sens. Actuators B Chem.* **2007**, *125*, 55.
[25] D. Routkevitch, T. Bigioni, M. Moskovits, J. M. Xu, *J. Phys. Chem.* **1996**, *100*, 14037.
[26] N. S. Ramgir, I. S. Mulla, K. P. Vijayamohanan, *Sens. Actuators B Chem.* **2005**, *107*, 708.
[27] H. Y. Yu, B. H. Kang, U. H. Pi, C. W. Park, S.-Y. Choi, G. T. Kim, *Appl. Phys. Lett.* **2005**, *86*, 253102.
[28] S. Omer, L. Forgách, R. Zelkó, I. Sebe, *Pharmaceutics* **2021**, *13*, 286.
[29] I. Robinson, S. Zacchini, L. D. Tung, S. Maenosono, N. T. K. Thanh, *Chem. Mater.* **2009**, *21*, 3021.
[30] J. Du, X. Lai, N. Yang, J. Zhai, D. Kisailus, F. Su, D. Wang, L. Jiang, *ACS Nano* **2011**, *5*, 590.
[31] H. Lin, H. Liu, X. Qian, S. Chen, Y. Li, Y. Li, *Inorg. Chem.* **2013**, *52*, 6969.
[32] N. Yang, Y. Liu, H. Wen, Z. Tang, H. Zhao, Y. Li, D. Wang, *ACS Nano* **2013**, *7*, 1504.
[33] Y. Guo, H. Liu, Y. Li, G. Li, Y. Zhao, Y. Song, Y. Li, *J. Phys. Chem. C* **2009**, *113*, 12669.
[34] J. Wang, N. Yang, H. Tang, Z. Dong, Q. Jin, M. Yang, D. Kisailus, H. Zhao, Z. Tang, D. Wang, *Angew. Chem.* **2013**, *125*, 6545.
[35] H. Ren, R. Yu, J. Wang, Q. Jin, M. Yang, D. Mao, D. Kisailus, H. Zhao, D. Wang, *Nano Lett* **2014**, *14*, 6679.
[36] J. Zhu, X. Yang, Z. Yang, D. Wang, P. Gao, J. Ye, *Adv. Funct. Mater.* **2018**, *28*, 1705425.
[37] J. Zhang, J. Wan, J. Wang, H. Ren, R. Yu, L. Gu, Y. Liu, S. Feng, D. Wang, *Angew. Chem.* **2019**, *131*, 5320.
[38] D. Wang, Z. Zhao, B. Shi, J. X. Wang, J. F. Chen, *ACS Appl. Mater. Interfaces* **2023**, *15*, 35358.
[39] J. Liu, Y. Wei, M. Chang, N. Wang, D. Wang, J. Wang, *AIChE J.* **2022**, *68*, e17522.
[40] J. Lv, Y. Zhao, G. Li, Y. Li, H. Liu, Y. Li, D. Zhu, S. Wang, *Langmuir* **2009**, *25*, 11351.
[41] L. Ji, X. Wang, Y. Jia, Q. Hu, L. Duan, Z. Geng, Z. Niu, W. Li, J. Liu, Y. Zhang, S. Feng, *Adv. Funct. Mater.* **2020**, *30*, 1910533.
[42] D. Li, R. B. Kaner, *J. Mater. Chem.* **2007**, *17*, 2279.
[43] K. K. Nanda, A. Maisels, F. E. Kruis, H. Fissan, S. Stappert, *Phys. Rev. Lett.* **2003**, *91*, 106102.
[44] Z. U. Abideen, J.-H. Kim, J.-H. Lee, J.-Y. Kim, A. Mirzaei, H. W. Kim, S. S. Kim, *J. Korean Ceram. Soc.* **2017**, *54*, 366.
[45] J. Moon, J.-A. Park, S.-J. Lee, T. Zyung, I.-D. Kim, *Sens. Actuators B Chem.* **2010**, *149*, 301.
[46] H. Tang, W. Chen, J. Wang, T. Dugger, L. Cruz, D. Kisailus, *Small* **2018**, *14*, 1703459.
[47] T. J. Xue, M. A. McKinney, C. A. Wilkie, *Polym. Degrad. Stab.* **1997**, *58*, 193.
[48] E. Fitzer, W. Frohs, M. Heine, *Carbon* **1986**, *24*, 387.
[49] I. Greenfeld, A. Arinstein, K. Fezzaa, M. H. Rafailovich, E. Zussman, *Phys. Rev. E* **2011**, *84*, 041806.
[50] S. L. Shenoy, W. D. Bates, H. L. Frisch, G. E. Wnek, *Polymer* **2005**, *46*, 3372.
[51] G. Vasilyev, M. Burman, A. Arinstein, E. Zussman, *Macromol. Mater. Eng.* **2017**, *302*, 1600554.
[52] M. Richard-Lacroix, C. Pellerin, *Macromolecules* **2015**, *48*, 4511.
[53] W. O. Siegl, *J. Org. Chem.* **1977**, *42*, 1872.
[54] R. A. Michelin, M. Mozzon, R. Bertani, *Coord. Chem. Rev.* **1996**, *147*, 299.
[55] G. Bresciani, L. Biancalana, G. Pampaloni, S. Zacchini, G. Ciancaleoni, F. Marchetti, *Molecules* **2021**, *26*, 7088.
[56] F. A. Bell, R. S. Lehrle, J. C. Robb, *Polymer* **1971**, *12*, 579.
[57] S. N. M. Salleh, M. Z. Abdullah, A. A. Wahab, *MATEC Web Conf.* **2014**, *13*, 04014.
[58] G. Y. Baek, H. S. Lee, J.-M. Jung, I.-T. Hwang, J. Shin, C.-H. Jung, J.-H. Choi, *J. Ind. Eng. Chem.* **2018**, *58*, 87.
[59] S. W. Zhang, *Wear of Metal by Rubber*, in Tribology and Interface Engineering Series, Vol. *47* (Ed: S. Zhang), Elsevier, Amsterdam **2004**, pp. 227–246.

[60] J. C. De Jesus, I. González, A. Quevedo, T. Puerta, *J. Mol. Catal. Chem.* **2005**, *228*, 283.
[61] T. Takahagi, I. Shimada, M. Fukuhara, K. Morita, A. Ishitani, *J. Polym. Sci. Part Polym. Chem.* **1986**, *24*, 3101.
[62] A. J. Wagner, G. M. Wolfe, D. H. Fairbrother, *Appl. Surf. Sci.* **2003**, *219*, 317.
[63] M. Cheng, H. Fan, Y. Song, Y. Cui, R. Wang, *Dalton Trans.* **2017**, *46*, 9201.
[64] L. Mi, W. Wei, S. Huang, S. Cui, W. Zhang, H. Hou, W. Chen, *J. Mater. Chem. A* **2015**, *3*, 20973.
[65] R. McKenzie, A. Knoll, B. Wang, S. Jadhav, R. Walker, A. Spirrison, *Eur. J. Inorg. Chem.* **2022**, *2022*, e202200074.
[66] G. Greczynski, L. X-R P S Hultman, *Prog. Mater. Sci.* **2020**, *107*, 100591.
[67] Y. Xu, J. Yu, J. Zhu, Q. Liu, H. Zhang, J. Liu, R. Chen, Y. Li, J. Wang, *Appl. Catal. B Environ.* **2022**, *316*, 121677.
[68] M. Huang, R. Ding, J. Yang, W. Shi, S. Shi, L. Chen, S. Liu, X. Yin, *J. Electrochem. Soc.* **2022**, *169*, 106507.
[69] F. Faupel, R. Willecke, A. Thran, Diffusion of Metals in Polymers **1998**.
[70] Z. Luo, S. Lim, Z. Tian, J. Shang, L. Lai, B. MacDonald, C. Fu, Z. Shen, T. Yu, J. Lin, *J. Mater. Chem.* **2011**, *21*, 8038.
[71] M. C. Biesinger, B. P. Payne, L. W. M. Lau, A. Gerson, R. St. C. Smart, *Surf. Interface Anal.* **2009**, *41*, 324.
[72] N. T. K. Thanh, N. Maclean, S. Mahiddine, *Chem. Rev.* **2014**, *114*, 7610.
[73] V. K. LaMer, R. H. T Dinegar, *J. Am. Chem. Soc.* **1950**, *72*, 4847.
[74] M. Jarcho, C. H. Bolen, M. B. Thomas, J. Bobick, J. F. Kay, R. H. Doremus, *J. Materi. Sci.* **1976**, *11*, 2027.
[75] J. A. Jiménez, M. In Sendova, *Solid State Commun.* **2011**, *151*, 720.
[76] K. Aihara, A. C. D. Chaklader, *Acta Metall.* **1975**, *23*, 855.
[77] B. B. Panigrahi, *Mater. Sci. Eng. A* **2007**, *460*, 7.
[78] T. J. Woehl, C. Park, J. E. Evans, I. Arslan, W. D. Ristenpart, N. D. Browning, *Nano Lett* **2014**, *14*, 373.
[79] R. M. Tromp, F. Legoues, P. S. Ho, *J. Vac. Sci. Technol. Vac. Surf. Films* **1985**, *3*, 782.
[80] W. H. Howard, *J. Appl. Polym. Sci.* **1961**, *5*, 303.
[81] D. Ehlich, H. Sillescu, *Macromolecules* **1990**, *23*, 1600.
[82] Y. Zhang, J. Zhang, *J. Mater. Res.* **2016**, *31*, 2233.
[83] J. Sehested, *J. Catal.* **2004**, *223*, 432.
[84] M. José-Yacamán, C. Gutierrez-Wing, M. Miki, D.-Q. Yang, K. N. Piyakis, E. Sacher, *J. Phys. Chem. B* **2005**, *109*, 9703.
[85] T. Hawa, M. R. Zachariah, *J. Aerosol Sci.* **2006**, *37*, 1.
[86] K. E. J. Lehtinen, M. R. Zachariah, *Phys. Rev. B* **2001**, *63*, 205402.
[87] P. Song, D. Wen, *J. Nanoparticle Res.* **2010**, *12*, 823.
[88] H. Li, M. Yuan, D. Tan, R. A. Susilo, H. Dong, Z. Chen, Y. Zhao, Y. Deng, B. Chen, *CrystEngComm* **2021**, *23*, 4152.
[89] W. Luo, W. G F E Hu, *Phys. B Condens. Matter* **2013**, *425*, 90.
[90] F. Ruffino, F. Giannazzo, *Crystals* **2017**, *7*, 219.
[91] A. Van Teijlingen, S. A. Davis, S. R. Hall, *Nanoscale Adv* **2020**, *2*, 2347.
[92] W. Thomson, *Proc. R. Soc. Edinb.* **1872**, *7*, 63.
[93] K. K. Nanda, F. E. Kruis, H. Fissan, *Phys. Rev. Lett.* **2002**, *89*, 256103.
[94] A. Moisala, A. G. Nasibulin, E. I. Kauppinen, *J. Phys.: Condens. Matter* **2003**, *15*, S3011.
[95] P. Kokmat, P. Surinlert, A. Ruammaitree, *ACS Omega* **2023**, *8*, 4010.
[96] C. J. Thambiliyagodage, S. Ulrich, P. T. Araujo, M. G. Bakker, *Carbon* **2018**, *134*, 452.
[97] S. Esconjauregui, C. M. Whelan, K. Maex, *Carbon* **2009**, *47*, 659.
[98] M. S. A. Rahaman, A. F. Ismail, A. Mustafa, *Polym. Degrad. Stab.* **2007**, *92*, 1421.
[99] E. Ruckenstein, H. Liu, *Ind. Eng. Chem. Res.* **1997**, *36*, 3927.
[100] K. G. Krishna, S. Parne, N. Pothukanuri, V. Kathirvelu, S. Gandi, D. Joshi, *Sens. Actuators Phys.* **2022**, *341*, 113578.
[101] M. I. Loría-Bastarrachea, W. Herrera-Kao, J. V. Cauich-Rodríguez, J. M. Cervantes-Uc, H. Vázquez-Torres, A. Ávila-Ortega, *J. Therm. Anal. Calorim.* **2011**, *104*, 737.
[102] I. NoorBatcha, R. R. Lucchese, Y. Zeiri, *J. Chem. Phys.* **1988**, *89*, 5251.
[103] R. D. Brancher, S. Stefanov, I. Graur, A. Frezzotti, *Vacuum* **2020**, *174*, 109166.
[104] Q. Feng, Y. Zeng, P. Xu, S. Lin, C. Feng, X. Li, J. Wang, *J. Mater. Chem. A* **2019**, *7*, 27522.
[105] Q. Feng, X. Li, J. Wang, A. M. Gaskov, *Sens. Actuators B Chem.* **2016**, *222*, 864.
[106] S. Brunauer, P. H. Emmett, E. Teller, *J. Am. Chem. Soc.* **1938**, *60*, 309.
[107] G. Horváth, K. Kawazoe, *J. Chem. Eng. Jpn.* **1983**, *16*, 470.
[108] X. Gao, T. Zhang, *Sens. Actuators B Chem.* **2018**, *277*, 604.

